JCTC Journal of Chemical Theory and Computation

Article

pubs.acs.org/JCTC

Variable-Cell Double-Ended Surface Walking Method for Fast Transition State Location of Solid Phase Transitions

Xiao-Jie Zhang and Zhi-Pan Liu*

Collaborative Innovation Center of Chemistry for Energy Material, Shanghai Key Laboratory of Molecular Catalysis and Innovative Materials, Key Laboratory of Computational Physical Science (Ministry of Education), Department of Chemistry, Fudan University, Shanghai 200433, China

Supporting Information

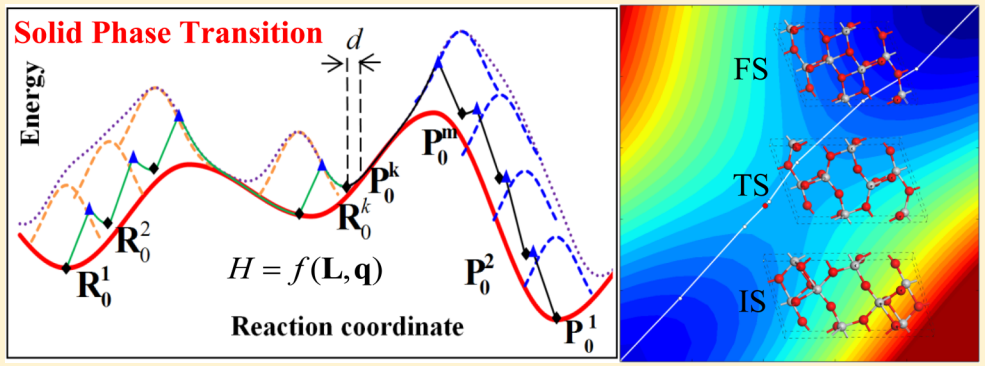

ABSTRACT: To identify the low energy pathway for solid-to-solid phase transition has been a great challenge in physics and material science. This work develops a new theoretical method, namely, variable-cell double-ended surface walking (VC-DESW) to locate the transition state (TS) and deduce the pathway in solid phase transition. Inherited from the DESW method (*J. Chem. Theory Comput.* **2013**, *9*, 5745) for molecular systems, the VC-DESW method implements an efficient mechanism to couple the lattice and atom degrees of freedom. The method features with fast pseudopathway building and accurate TS location for solid phase transition systems without requiring expensive Hessian computation and iterative pathway optimization. A generalized coordinate, consisting of the lattice vectors and the scaled atomic coordinates, is designed for describing the crystal potential energy surface (PES), which is able to capture the anisotropic behavior in phase transition. By comparing with the existing method for solid phase transition in different systems, we show that the VC-DESW method can be much more efficient for finding the TS in crystal phase transition. With the combination of the recently developed unbiased stochastic surface walking pathway sampling method, the VC-DESW is further utilized to resolve the lowest energy pathway of SiO_2 α-quartz to quartz-II phase transition from many likely reaction pathways. These new methods provide a powerful platform for understanding and predicting the solid phase transition mechanism and kinetics.

1. INTRODUCTION

Solid phase transition is an important phenomenon in nature. Being different from reactions in a finite system, e.g., molecules and clusters, solid phase transition is much more complex, involving collective atom movement together with the change of crystal lattice (e.g., graphite to diamond). To identify the solid transition pathway and resolve the mechanism have long been huge challenges with regard to both theory and experiment. From a theoretical point of view, there are two fundamental difficulties in exploring the potential energy surface (PES) of a solid. First, the reaction barrier in solid phase transition can be very high as a number of chemical bonds form/break simultaneously from one crystal phase to another. Second, the reaction coordinate in the phase transition is generally nonintuitive and hard to guess *a priori*. The traditional finite-temperature molecular dynamics (MD) methods and single-ended transition state (TS) searching methods[1,2] are thus not applicable for solid phase transition.

The crystal phase transition can be simplified as a homogeneous phase transition, which could mimic the reaction at certain high pressure limits or at the initial nucleation stage. This is shown schematically in Figure 1a, where the lattices and atoms displace from a crystal structure of one phase to another crystal structure of a new phase. The key question for solid phase transition is thus how to identify the lowest energy pathway, where the lattice and atom correspondence between phases can be established to understand the phase transition mechanism and kinetics.

Traditionally, solid phase transition was often analyzed using the phenomenological Landau-type theory in combination with

Received: July 6, 2015
Published: September 25, 2015

DOI: 10.1021/acs.jctc.5b00641
J. Chem. Theory Comput. 2015, 11, 4885−4894

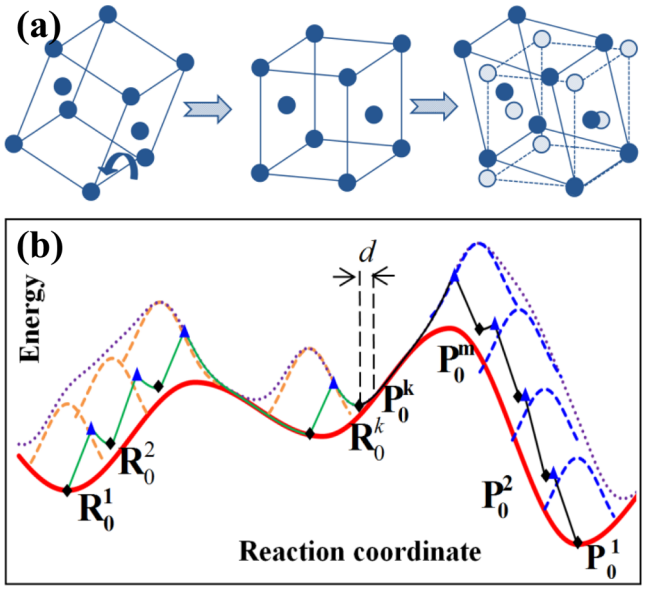

Figure 1. (a) Illustration of the homogeneous crystal phase transition reaction that can be decomposed into two steps: (i) crystal rotation and (ii) crystal deformation including both lattice and atom displacements. (b) 1-D scheme of the DESW method in building the pseudopathway (also see ref 3).

group theory,[4] which, however, lacks atomic detail of the phase transition. With the advent of computational simulation, in the past decades many elegant atomistic simulation methods have been developed to treat solid phase transition. The Parrinello–Rahman MD (PR-MD) simulation at the NpT ensemble is able to explore crystal phase space at finite temperature and pressure.[5,6] The method was applied to reveal the phase transition pathway in simple crystal systems, such as AgI[7] and Si.[8] The rate of phase transition can be analyzed using transition path sampling.[9−11] For crystal phase transition with high barriers, the PR-MD method is, however, not efficient for the exponential dependence of the rate on the barrier. To overcome this shortcoming, the biased MD simulation method, metadynamics,[12−14] was developed to explore the phase transition pathways. By filling Gaussian bias potentials on all lattice degrees of freedom, metadynamics is able to drive phase transition, and the method has been applied to some important systems, such as SiO_2,[13] $MgSiO_3$,[15] and CO_2.[16] However, because the method lacks of an efficient mechanism to couple the lattice and atom movement, it is generally not applicable in systems involving a complex pattern of atomic movement that is not explicitly driven by the lattice deformation (e.g., the phase transition with large changes on atomic coordinates but only small changes in lattice coordinates).

Compared to the MD based approaches, the TS searching method is less computationally demanding, which, however, requires additional knowledge of the reaction coordinate. For solid states, the reaction coordinate is not intuitive due to the many possible representations of the crystal lattice. This is different from the molecular reaction where TS-location approaches were widely utilized even under complex reaction conditions, e.g., those in heterogeneous catalysis.[17,18] To capture the reaction coordinate in solid phase transition, it has to assume an initial (IS) and a final state (FS) of crystal phases. Only with this IS/FS pair, the double-ended TS location method can be utilized to locate the TS and the pathway. Since there are apparently many possible combinations of IS/FS pairs for a crystal phase transition, a trial-and-error approach has to be taken to search for a number of likely pathways in order to identify the lowest energy pathway.

The double-ended TS location method for crystal phase transition has been available only recently and is still in development. On the basis of the nudged-elastic-band (NEB) method, Trinkle et al.[19] developed a stepwise TS searching method to study the transition metal Ti α-to-ω phase transition. In their method, the conventional NEB was performed to treat only atomic coordinates, and additional optimization steps were utilized to relax the lattice parameters in response to the induced stress.[19,20] Caspersen and Carter developed a lattice-version NEB method, named solid state NEB (SSNEB), with the NEB spring applied only on the lattice coordinate,[21] while the atomic fractional coordinate is fixed in SSNEB pathway iterations. More recently, Sheppard et al.[22] developed the generalized SSNEB (G-SSNEB) method by introducing an isotropic scaling parameter to couple the atomic and lattice degrees of freedom, where the Cartesian coordinate and the lattice strain are combined to describe the PES. G-SSNEB was shown to identify a lower energy pathway for CdSe crystal phase transition[22] compared to the SSNEB method provided with the same IS and FS.

Recently, we developed an automated approach to identify the low energy pathway of molecular reactions based on stochastic surface walking (SSW)[23,24] pathway sampling and the double-ended surface walking (DESW) TS location.[3] The SSW sampling explores the likely pathways on PES starting from one reactant and produces a database of reactant and product pairs (IS/FS pairs). The subsequent location of the TS linking these IS/FS pairs would allow the finding of the lowest energy pathways. Not limited to molecular systems, this new pathway sampling method can be extended to study crystal phase transition as demonstrated recently in a number of crystal systems[24−26] including ZrO_2 tetragonal phase to monoclinic phase.[26] While the SSW pathway sampling for the crystal method has been reported and benchmarked in detail,[24] here we will present the detailed algorithm of the variable-cell DESW method (VC-DESW), which is designed to quickly locate the TS of crystal phase transition.

Developed upon the DESW method, the VC-DESW method is able to establish a pseudopathway linking two crystal phases with varied lattice parameters and then locate the TS accurately using the pseudopathway information. The method designs a generalized coordinate for describing the crystal PES, which consists of the lattice vectors and the scaled atomic coordinates. We show that this generalized coordinate system is able to produce soft modes containing both lattice and atom degrees of freedom and thus efficiently couple the lattice displacement and the atom movement in solid phase transition. We apply the VC-DESW method to several example systems with complex phase transition pathways, and the high efficiency of the method is demonstrated by comparing in detail with the existing methods.

2. METHODS

2.1. Overview of the DESW Algorithm. In order to elaborate the VC-DESW method, we first introduce briefly the main framework of the DESW method. The DESW method is targeted to quickly locate the TS of molecular reactions.[3] The DESW method includes two main parts, i.e., pseudopathway building and TS location.

DOI: 10.1021/acs.jctc.5b00641
J. Chem. Theory Comput. 2015, 11, 4885−4894

2.1.1. Pseudopathway Building. The central part of the DESW method is to quickly build a pseudopathway linking IS and FS. As illustrated in Figure 1b, the algorithm defines two structure images, **R** and **P**, initiating from the IS and the FS basins, which walk toward each other on the PES. "Surface walking" is carried out by repeated Gaussian function addition and local relaxation. $\mathbf{R_0}^i$ and $\mathbf{P_0}^i$ are the structure images on the pseudopathway obtained after each local optimization, where the superscript i indicates the sequence of the images counting from each side. The two sides will eventually meet with each other (measured by the distance d in Figure 1b), which establishes a psudopathway connecting IS with FS.

The walking direction is critical in DESW method. The initial walking directions at $\mathbf{R_0}^i$ (or $\mathbf{P_0}^i$) are updated dynamically as the two sides get close to each other, as given by the coordinate difference vector in eq 1. Obviously, the direction always points toward each other.

$$\mathbf{N_i}^{\mathrm{init,R}} = \frac{\mathbf{P_0}^i - \mathbf{R_0}^i}{||\mathbf{P_0}^i - \mathbf{R_0}^i||};\ \mathbf{N_i}^{\mathrm{init,P}} = \frac{\mathbf{R_0}^{i+1} - \mathbf{P_0}^i}{||\mathbf{R_0}^{i+1} - \mathbf{P_0}^i||} \tag{1}$$

These initial directions will be further refined/optimized using the (un)biased rotation of the constrained-Broyden dimer rotation (CBD) method,[27] and at convergence, $\mathbf{N_i}^{\mathrm{init,R}}$ (or $\mathbf{N_i}^{\mathrm{init,P}}$) is optimized to $\mathbf{N_i}^{\mathrm{R}}$ (or $\mathbf{N_i}^{\mathrm{P}}$). The optimized $\mathbf{N_i}$ should be close to or equal to one eigenvector of the Hessian matrix, being a good approximation to the reaction coordinate. In this way, the walking direction is adaptive to the shape of PES.

With $\mathbf{N_i}$ being determined, the DESW method translates the structure image from $\mathbf{R_0}^i$ to $\mathbf{R_t}^i$ by adding a new Gaussian centering at $\mathbf{R_0}^i$ and performs the local relaxation to yield $\mathbf{R_0}^{i+1}$. The real PES (V_{real} at $\mathbf{R_t}^i$) is modified by adding a bias potential V_G as eq 2. The V_G is a summation of all previously added Gaussians, as shown in eq 3. The $\mathbf{N_i}$ defines the direction where the Gaussian potential will be added, which is to prevent $\mathbf{R_t}^i$ falling back to the minimum basins during the structure translation uphill toward TS region. Each Gaussian function has two parameters, the height w_i and the width ds. The Gaussian height is automatically adjusted during pathway building, whereas the Gaussian width is left as an input parameter, being set as 0.2 Å by default.

$$V = V_{real} + V_G \tag{2}$$

$$V_G = \sum_{i=1}^{k} v_i = \sum_{i=1}^{k} w_i \exp\left(-\frac{[(\mathbf{R_t}^i - \mathbf{R_0}^i)\cdot\mathbf{N_i}]^2}{2ds^2}\right) \tag{3}$$

2.1.2. TS Location. Starting from the highest energy structure image (i.e., $\mathbf{P_0}^m$ as illustrated in Figure 1b) in the pseudopathway, the single-ended TS location method can be utilized to exactly locate the TS (this corresponds to the highest energy TS if there are multiple TSs along the pathway). In DESW, we utilize the CBD method,[28] a modified version of the dimer method,[29,30] to locate the TS, which contains two independent modules, namely, the dimer rotation and the translation. The dimer rotation is carried out by the numerical constrained Broyden dimer rotation method, which can identify the reaction coordinate, e.g., an associated eigenvector of Hessian matrix with the negative eigenvalue. It is then possible to translate the structure gradually toward the TS along the reaction coordinate using a Quasi-Newton Broyden method. The translation force $\mathbf{F}_t$ is obtained from eq 4 by modifying the total force **F**, where the force component along the reaction coordinate ($\mathbf{F}_p$) is reversed in direction; a tunable factor $\lambda(\lambda \in (1,2))$ controls the step size of the translation.

$$\mathbf{F}_t = \mathbf{F} - \lambda\mathbf{F}_p = \mathbf{F} - \lambda(\mathbf{F}\cdot\mathbf{N})\mathbf{N} \tag{4}$$

2.2. Algorithm of the VC-DESW Method. The basic framework of the VC-DESW remains the same as that of the DESW: both contain the same modules, the pseudopathway building and the TS location. Below we focus on the new features added in the VC-DESW implementation, which are related to the lattice degrees of freedom. The generalized coordinate that includes both lattice and atom degrees of freedom is first introduced and derived. It is then followed by the algorithm to identify the reaction coordinate in crystal phase transition. The comparison between VC-DESW with G-SSNEB is also detailed at the end of this section.

2.2.1. Generalized Coordinate. For a periodic crystal with n atoms per unit cell, the total degrees of freedom are $3n + 3$, including six degrees of freedom of the lattice and $3n - 3$ degrees of freedom of the atom. From one crystal phase to another, the TS corresponds to the first-order saddle point (all the forces diminish at the TS with one and only one negative normal mode) along the minimum energy pathway on the PES spanned by the total $3n + 3$ degrees of freedom. In order to identify the TS, it is essential to construct a generalized coordinate to describe the PES of the crystal, which should have an efficient mechanism to couple the lattice and atom degrees of freedoms.

For crystal, the fractional coordinate **q** of atoms can be related to the Cartesian coordinate **R** and the lattice matrix **L**

$$\mathbf{q} = \mathbf{L}^{-1}\mathbf{R} \tag{5}$$

While either **q** or **R** can be a possible choice for atomic coordinate, the fractional coordinate **q** is preferable as it is rotationally invariant, a desired property when matching two crystal structures. The potential energy of the system is then described by the enthalpy H, a function of the lattice vector **L** and the fractional coordinate **q**.

$$H = f(\mathbf{L}, \mathbf{q}) \tag{6}$$

It is noted that the lattice vector **L** is in real distance units, e.g., in Å, but the fractional coordinate **q** is a relative quantity in between 0 and 1. For the numerical stability in structure optimization, it is essential to scale the fractional coordinate to let its magnitude be compatible with the magnitude of **L**. This can be treated using eqs 7−9.

$$\mathbf{G} = \mathbf{L}_r{}^T\mathbf{L}_r \tag{7}$$

$$\mathbf{S} = \mathbf{G}^{1/2} \tag{8}$$

$$\mathbf{q}' = \mathbf{S}\mathbf{q} \tag{9}$$

Specifically, we consider a rotational invariant matrix **G**, the metric tensor of a reference lattice $\mathbf{L}_r$ in eq 7 (the choice of $\mathbf{L}_r$ will be described in eq 14), and define the square root of the metric tensor as a scaling matrix, **S**. The metric tensor **G** was suggested previously by Souza and Martins[32] as a dynamic variable for variable-cell MD. The **S** can be obtained by Cholesky decomposition of **G** (eq 8). The fractional coordinate can then be transformed to a new set of scaled coordinate, $\mathbf{q}'$, the magnitude of which is now compatible with the lattice length. We therefore define the generalized coordinate **Q** as

$$\mathbf{Q} = \{\mathbf{L}, \mathbf{q}'\} \tag{10}$$

DOI: 10.1021/acs.jctc.5b00641
J. Chem. Theory Comput. 2015, 11, 4885−4894

Accordingly, the force acting on the generalized coordinate $\mathbf{Q}$ can be written as

$$\mathbf{F} = \{\mathbf{F}_L, \mathbf{F}_{q'}\} \tag{11}$$

where $\mathbf{F}_{q'}$ and $\mathbf{F}_L$ can be derived as

$$\mathbf{F}_{q'} = \frac{\partial H}{\partial \mathbf{q}'} = (\mathbf{S}^T)^{-1}\mathbf{L}^T\mathbf{F} \tag{12}$$

$$\mathbf{F}_L = -\frac{\partial H}{\partial \mathbf{L}} = -\Omega[(\sigma - p_{ext})(\mathbf{L}^T)^{-1}] \tag{13}$$

The forces on the lattice vectors $\mathbf{F}_L$ can be related to the stress tensor σ of the lattice,[21,24] where Ω is the volume of the lattice, and p_{ext} is the external pressure.

As for the scaling matrix $\mathbf{S}$, it must be predefined and kept as constant in building the pseudopathway. While there are many possible choice of $\mathbf{S}$ (or $\mathbf{L}_r$ and $\mathbf{G}_r$; see eqs 7−10), e.g., $\mathbf{L}_r$ being set as the $\mathbf{L}$ of the IS, we here define $\mathbf{G}_r$ (eq 14) to be the geometrical average of the metric tensor $\mathbf{G}$ for IS ($\mathbf{L}_{IS}$) and the FS lattice ($\mathbf{L}_{FS}$).

$$\mathbf{G}_r = (\mathbf{G}_{IS} + \mathbf{G}_{FS})/2 \tag{14}$$

We found that this choice of $\mathbf{G}_r$ is efficient for many crystal phase transition systems examined in the group[25,33−35] (also see section 3). The scaling matrix $\mathbf{S}$ and the generalized coordinate $\mathbf{Q}$ can then be derived using eqs 9−10.

We would like to emphasize two properties of the scaled fractional coordinate of atoms. First, the scaled coordinate is invariant with respect to the lattice rotation. The lattice rotation, although generally involved in the crystal phase transition (see Figure 1a), has no effective contribution to the energy profile of the pathway. By removing the lattice rotation contribution, the Euclidean distance between the IS and FS can be maximally minimized to achieve the best structure match, which speeds up pathway building in the VC-DESW method.

Second, the scaled fractional coordinate can describe better the coupling between the atom and lattice, leading to the soft mode related to lattice displacement. We illustrate this using a TiO_2 crystal as illustrated in Figure 2a, which plots the energy function as the change of a lattice vector of $\mathbf{L}_a$ length (along a axis). The red curve represents the energy function where the Cartesian coordinate is kept fixed during the change of $\mathbf{L}_a$, while the black curve is the one with the fractional coordinate being fixed. The curvature corresponding to the lattice displacement, C, can be thus visualized, which is the second derivative of enthalpy H with respect to the length of $\mathbf{L}_a$ (eq 15).

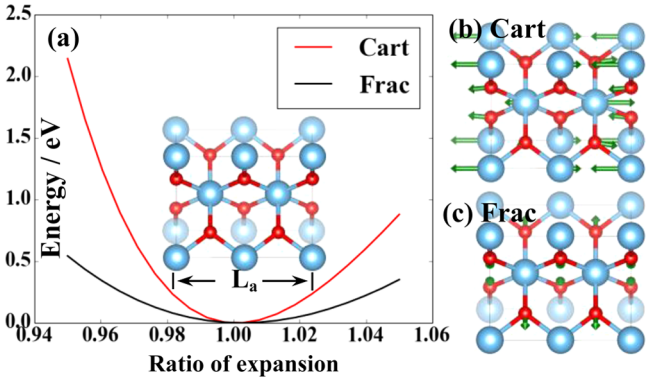

Figure 2. Plot of potential energy vs lattice expansion along the a axis of TiO_2 anatase by either fixing the fractional coordinates (black curve) or fixing the Cartesian coordinates of atoms (red curv). (b and c) are the corresponding force vectors (green arrows) on atoms due to lattice expansion. From the plot, it can be deduced that the curvature with the fixed Cartesian coordinate (32.68 eV/Å^2) is much larger than that with the fixed fractional coordinate (11.17 eV/Å^2). The interaction in TiO_2 is described by the Matsui-Akaogi empirical potential.[31]

$$C = \frac{\partial^2 H}{\partial \mathbf{L}_a^{\,2}} \tag{15}$$

We can see that the curvature is much smoother in the case of the fractional coordinate, and consistently, the force vectors acting on the atoms are distributed uniformly on atoms inside the crystal lattice as shown in Figure 2b. This couples effectively the lattice displacement with the atom movement inside the crystal cell. By contrast, in the case of the Cartesian coordinate, the change of the lattice vector affects mainly the atoms at the edge of the cell, where the force vectors have the largest distribution (see Figure 2c).

2.2.2. Reaction Coordinate. The VC-DESW method utilizes the numerical CBD rotation method to identify the normal mode that is associated with the reaction coordinate. In the dimer rotation, two structural images, $\mathbf{Q}_0$ and $\mathbf{Q}_1$, are generated with a fixed spacing dQ according to the forward finite difference algorithm[29] expressed in eqs 16−18. The dimer length dQ is typically set as 0.01.

$$\mathbf{Q}_1 = \mathbf{Q}_0 + \mathbf{N}dQ \tag{16}$$

$$\mathbf{Q}_0 = \{\mathbf{L}_0, \mathbf{q}_0'\}$$

$$\mathbf{Q}_1 = \{\mathbf{L}_1, \mathbf{q}_1'\} \tag{17}$$

$$\mathbf{N} = \{\mathbf{N}_L, \mathbf{N}_{q'}\} \tag{18}$$

The initial input of $\mathbf{N}$ is $\mathbf{N}_{init}$ from eq 1, and the dimer rotation can optimize $\mathbf{N}$ by minimizing the rotational force acting on the dimer, which is the difference of the vertical force $\mathbf{F}_v$ (eq 19) acting on the image $\mathbf{Q}_1$ and $\mathbf{Q}_0$.

$$\mathbf{F}_v = \mathbf{F}_1 - \mathbf{F}_0 - [(\mathbf{F}_1 - \mathbf{F}_0)\cdot\mathbf{N}]\mathbf{N} \tag{19}$$

In the positive curvature region (near the minimum basins), the (unbiased) dimer method tends to converge to the softest normal mode in the system, which is generally not the reaction coordinate we are interested in. To retain the reaction information from $\mathbf{N}_{init}$, the biased CBD rotation method is utilized instead at the minimum basins, which adds an extra quadratic potential V_N at $\mathbf{Q}_1$ (eqs 20−21). The force acting on $\mathbf{Q}_1$ is thus modified as shown in eqs 22−23. The details of the biased CBD method have been described previously.[27]

$$V_1 = V_1^{real} + V_N \tag{20}$$

$$V_N = -\frac{a}{2}[(\mathbf{Q}_1 - \mathbf{Q}_0)\cdot\mathbf{N}_{init}]^2 = -\frac{a}{2}[dQ(\mathbf{N}_t\cdot\mathbf{N}_{init})]^2 \tag{21}$$

$$\mathbf{F}_N = -\frac{\partial V_N}{\partial \mathbf{Q}_1} = a[dQ(\mathbf{N}_t\cdot\mathbf{N}_{init})\mathbf{N}_{init}] \tag{22}$$

$$\mathbf{F}_1 = \mathbf{F}_1^{real} + \mathbf{F}_N \tag{23}$$

We noted that the efficiency is in fact similar for CBD rotation for optimizing $\mathbf{N}$ with and without the lattice components. This is due to the fact that the degrees of

DOI: 10.1021/acs.jctc.5b00641
J. Chem. Theory Comput. 2015, 11, 4885−4894

Table 1. Results for Locating the Solid Phase Transition TS Using the VC-DESW Method and the G-SSNEB Method[a]

				VC-DESW[b]			G-SSNEB method[d]		
system	N_{atom}	dist. (Å)	E_a (E_a^{est}) (eV)	N_{path}	N_{CBD}	N_{tot}[c]	N_{img}	$N_{F\text{-}img}$	N_{all}
TiO_2-B-to-anatase	24	4.01	0.86 (0.96)	116	78	194(149)	5/10	44/38	220/380
rutile-to-TO_2-II	48	6.11	3.66 (3.66)	199	27	228(346)	6/10	50/68	300/680

[a]The listed data include the number of atoms per unit cell (N_{atom}), the Euclidean distance measured by the generalized coordinate (dist.), and the energy barrier (E_a). The estimated barrier (E_a^{est}) from the VC-DESW pseudopathway is also listed in parentheses together with the energy barrier for comparison. [b]N_{path} and N_{CBD} are the force and energy evaluation steps in the VC-DESW pathway building and CBD for TS location, respectively. N_{tot} is the sum of N_{path} and N_{CBD}. [c]The data in parentheses are the additional force/energy evaluation steps required to generate the reaction pathway by extrapolating TS toward IS/FS. [d]Two calculations with different NEB images (N_{img}) have been tested in each example: 5 and 10 N_{img} for TiO_2-B-to-anatase; 6 and 10 for rutile-to-TiO_2-II. Data for the force and energy evaluation steps per image $N_{F\text{-}img}$ and the overall force and energy evaluation steps N_{all} are listed.

freedom of the atom are generally much larger and dominate the computational cost in the TS search.

2.2.3. Comparison between VC-DESW and G-SSNEB. It is of interest to compare the VC-DESW method with the G-SSNEB method with the algorithm. Both methods belong to the double-ended TS location method and are targeted to identify the TS of solid phase transition. The G-SSNEB is originated from the NEB method, whereas the VC-DESW method is based on the DESW method. We have shown previously that the DESW method establishes only a pseudopathway but that the NEB method can converge to the minimum energy pathway (MEP) via iterative pathway optimization. The DESW method is more efficient if we are only interested in the TS. The obtained peudopathway in DESW is not the MEP but generally gets close to the MEP at the TS regions. These general differences are still valid when comparing VC-DESW with G-SSNEB.

Apart from the above differences, we would like to emphasize that the generalized coordinate utilized in the VC-DESW method is distinct from that utilized in the G-SSNEB method. In the G-SSNEB method, the generalized coordinate combines the scaled lattice vector with the Cartesian coordinate of atom ($\mathbf{R}$). The reaction coordinate along the NEB pathway is defined as

$$\Delta\mathbf{R}_{tot} = \{J\varepsilon, \Delta\mathbf{R}\} \tag{24}$$

where ε is the lattice strain, which is the percentage of the lattice deformation from the initial lattice $\mathbf{L}$ to the new lattice $\mathbf{L}^{new}$.

$$\varepsilon = \mathbf{L}^{-1}\cdot(\mathbf{L}^{new} - \mathbf{L}) \tag{25}$$

J is a Jacobian constant being constructed as a function of the volume of a reference cell (Ω) and the number of atoms (n) in the cell.

$$J = \Omega^{1/3}n^{1/6} \tag{26}$$

By contrast, the reaction coordinate in the VC-DESW method can be written as eq 27, the difference between a new coordinate $\mathbf{Q}_1$ and an original coordinate $\mathbf{Q}_0$.

$$\Delta\mathbf{Q} = \mathbf{Q}_1 - \mathbf{Q}_0 = \{\Delta\mathbf{L}, \Delta\mathbf{q}'\} \tag{27}$$

The reaction coordinate $\Delta\mathbf{Q}$ can be transformed to the expression similar to that defined in the G-SSNEB by multiplying two matrixes, $\mathbf{L}$ and $\mathbf{S}^{-1}$, as follows.

$$\mathbf{L}\mathbf{S}^{-1}\Delta\mathbf{Q} = \{\mathbf{L}\mathbf{S}^{-1}\Delta\mathbf{L}, \mathbf{L}\mathbf{S}^{-1}\Delta\mathbf{q}'\} \approx \{\mathbf{L}\varepsilon, \Delta\mathbf{R}\} \tag{28}$$

The above equation utilizes the approximation that $\mathbf{S}$ is equal to $\mathbf{L}$ (since $\mathbf{S}$ is the square root of the matrix tensor $\mathbf{L}_r^T\mathbf{L}_r$ and $\mathbf{L}_r$ can be set as $\mathbf{L}$ of IS). By comparing eq 28 with eq 24, we found that the reaction coordinate in VC-DESW would be similar to that in G-SSNEB if the $\mathbf{L}$ is replaced by the Jacobian J (in multiplying the strain). Because $\mathbf{L}$ is a matrix, instead of a constant, with varied lengths at different lattice vector directions, the multiplication of $\mathbf{L}$ to the strain acts an anisotropic scaling on different lattice vector directions. From our examples shown below, we found that this anisotropic scaling is essential to identify the normal mode composing of both lattice and atom degrees of freedom that describes the reaction coordinate of the crystal phase transition. However, the anisotropic scaling could be less efficient for some long supercell calculations as discussed previously.[22] For VC-DESW, we have tested the TS location performance in different supercells and found that the cubic-like supercell generally provides the better performance by up to 35% in pseudopathway building, and thus, the supercell with one dimension being too long should be avoided in practice.

3. RESULTS AND DISCUSSION

3.1. Examples for TS Location. To illustrate the efficiency of the VC-DESW method, we here examined two TiO_2 solid phase transition systems, namely, the TiO_2-B (symmetry $C2/m$, a = 6.48 Å, b = 3.75 Å, c = 12.16 Å, $\alpha = \gamma = 90°$, β = 75.8°, and Z = 4) to anatase ($I4_1/amd$, a = 3.77 Å, b = 3.77 Å, c = 9.57 Å, $\alpha = \beta = \gamma = 90°$, and Z = 4) transition and the TiO_2-II ($Pbnm$, a = 4.58 Å, b = 5.58 Å, c = 4.93 Å, $\alpha = \beta = \gamma = 90°$, and Z = 4) to rutile ($P4_2/mnm$, $a = b$ = 4.65 Å, c = 2.96 Å, $\alpha = \beta = \gamma = 90°$, and Z = 2) transition. These TiO_2 systems are important in applications, for example, as photocatalysts for water splitting. The partial phase transition can lead to the formation of biphase junction, which is known to boost the photoactivity.[36,37] In our previous work, the lowest energy transition pathway of these two TiO_2 systems have been determined based on the pathways from SSW crystal pathway sampling.[24,34] In these lowest energy pathways, the IS/FS structures are generally not the Bravais lattice of the corresponding crystal phase, indicating that predicting the reaction coordinate is difficult in complex phase transition systems. Here, we analyze the efficiency of VC-DESW for finding the TS of crystal phase transition, which is compared with that using the G-SSNEB method.[38] In both cases, the same IS/FS pair is utilized.

These two TiO_2 systems are representatives of complex solid phase transition with large displacements on both lattice and atom coordinates. The Euclidean distance as calculated from the generalized coordinate (eq 10) are 4.01 and 6.11 Å for the two systems and thus much longer than the simple phase transition of the metal system, e.g., from alpha-to-omega in metal Ti (<2 Å). The TiO_2-B-to-anatase pathway is a direct

DOI: 10.1021/acs.jctc.5b00641
J. Chem. Theory Comput. 2015, 11, 4885−4894

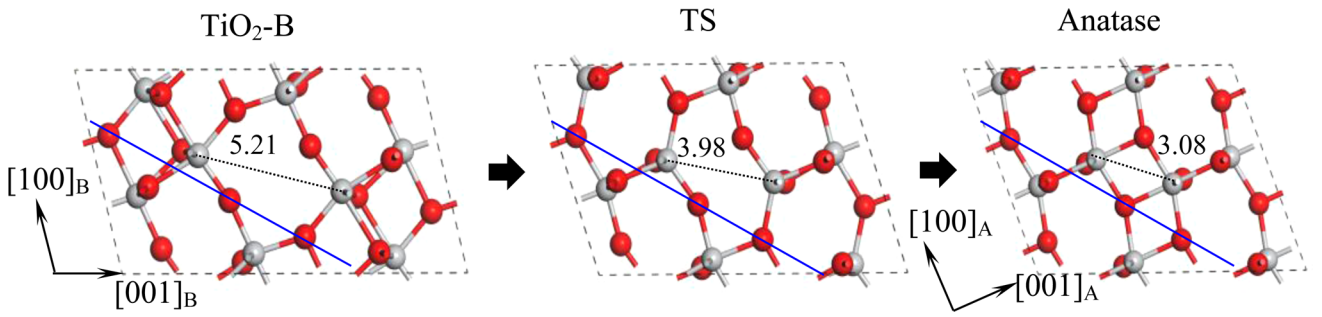

Figure 3. IS, TS, and FS structures along the TiO_2-B-to-anatase phase transition pathway. The atomic habit plane edges, TiO_2-B $(\bar{2}01)$ and anatase (103), are denoted by blue lines. The labeled Ti−Ti distance is in Å. Ti atom, gray ball; O atom, red ball.

transition pathway without an intermediate, and the unit cell in the pathway contains 24 atoms (8 TiO_2). The rutile-to-TiO_2-II pathway involves an intermediate structure (Baddeleyite, $P2_1/c$) in the lowest energy pathway as discussed previously,[24] and we selected a large unit cell for this pathway, i.e., 48 atoms per unit cell (16 TiO_2).

All of the force and energy evaluations were performed using a first-principles density functional theory (DFT) plane wave method as implemented in the VASP package.[39,40] The kinetic energy cutoff utilized was 500 eV, and the ionic core electrons were described using the projector augmented wave (PAW) pseudopotential.[41] The electron exchange and correlation effects are described by the GGA-PBE functional.[42] The first Brillouin zone was sampled using the Monkhorst−Pack scheme[43] with a (4 × 4 × 4) for TiO_2-B-to-anatase and a (2 × 2 × 2) for rutile-to-TO_2-II phase transition systems. The convergence criteria of force were set as 0.05 eV/Å for each atomic degree of freedom, while that of the stress was 0.05 GPa for TiO_2-B-to-anatase and 0.15 GPa for rutile-to-TiO_2-II.

In the VC-DESW, the Gaussian width utilized was set as 0.3 Å. In the G-SSNEB, we have tested different numbers of images (N_{img} in Table 1) along the NEB string to establish the pathway, and the climbing image was employed to accurately locate the TS. Calculations with a small number of NEB images are usually able to quickly locate TS but may lose the pathway resolution, while those with large NEB images can be utilized to converge the reaction pathway close to the MEP. The spring constant of the G-SSNEB method was 5.0 eV/Å. The structural optimization of G-SSNEB was performed by the fast inertial relaxation engine (FIRE) method[44] with the maximum allowed step size as 0.2 Å and the time step as 0.1.

Our main results are summarized in Table 1. Both the VC-DESW and the G-SSNEB can locate accurately the correct TS for these systems. From these selected examples, we show that, if only we are only interested in the highest energy TS, then the VC-DESW is more efficient than the G-SSNEB method by up to 30% depending on the number of NEB images utilized in G-SSNEB. In the following, we will elaborate these results by analyzing the TS structure and the pathways from two methods.

3.1.1. TiO_2-B-to-Anatase Phase Transition. This phase transition follows the diffusionless Martensitic phase transition mechanism with a crystallographic orientation relationship, $(\bar{2}01)_B//(103)_A$ and $[010]_B//[010]_A$,[25] which has been proved by comparing the theoretical results with the experimental HRTEM pictures.[25] We have shown previously that the phase transition initiates from the TiO_2-B $(\bar{2}01)$ crystal plane involving the collective layer-by-layer gliding along the $[\bar{1}0\bar{2}]$ direction. The located TS together with the IS and the FS for the TiO_2-B-to-anatase phase transition is shown in Figure 3. The phonon spectrum of the TS is shown in Supporting Information, exhibiting one and only one imaginary eigenvalue in the first Brillouin zone.

As shown in Table 1, the VC-DESW takes 194 energy and force evaluation steps to locate the TS, while it requires 220−380 steps (220 steps with 5 NEB images and 380 steps with 10 NEB images) in the G-SSNEB. (In practice, G-SSNEB can run in parallel efficiently, e.g., each image on a number of nodes, and the actual wall-clock time for each job depends on computational resources.) To understand the procedure of VC-DESW, we have plotted the VC-DESW trajectory and compare it with the converged G-SSNEB pathways in Figure 4. The *xy* plane of Figure 4 is constructed by the IS, TS, and FS, and the *z* axis measures the deviation of the structure away from the IS−TS−FS plane. The *x*/*y* unit vectors and the values in the *z* axis are defined using eqs 29−31. This type of plot has been utilized in the previous work for illustrating the reaction pathways.[3]

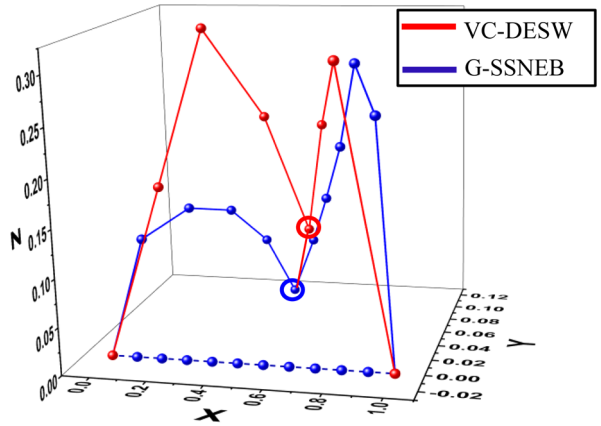

Figure 4. VC-DESW trajectory (red line) together with the pathways (blue) from the G-SSNEB method. Dotted blue line, the initial pathway via the linear interpolation; blue line, the converged G-SSNEB pathway after 68 iterations.

Figure 4 shows that the MEP (blue line) obtained from G-SSNEB is curved, being far away from the linear interpolation between the IS and FS (the blue dotted line). It takes 38 iterations in G-SSNEB (10 NEB images) to optimize the pathway to the MEP. However, the pseudopathway obtained by the VC-DESW method (red line) is close to the converged MEP from G-SSNEB, although no iterative optimization of the pathway is performed in VC-DESW. The maximal energy position along the VC-DESW pathway (red circle) is close to the true TS (blue circle). The estimated barrier is 0.96 eV,

DOI: 10.1021/acs.jctc.5b00641
J. Chem. Theory Comput. 2015, 11, 4885−4894

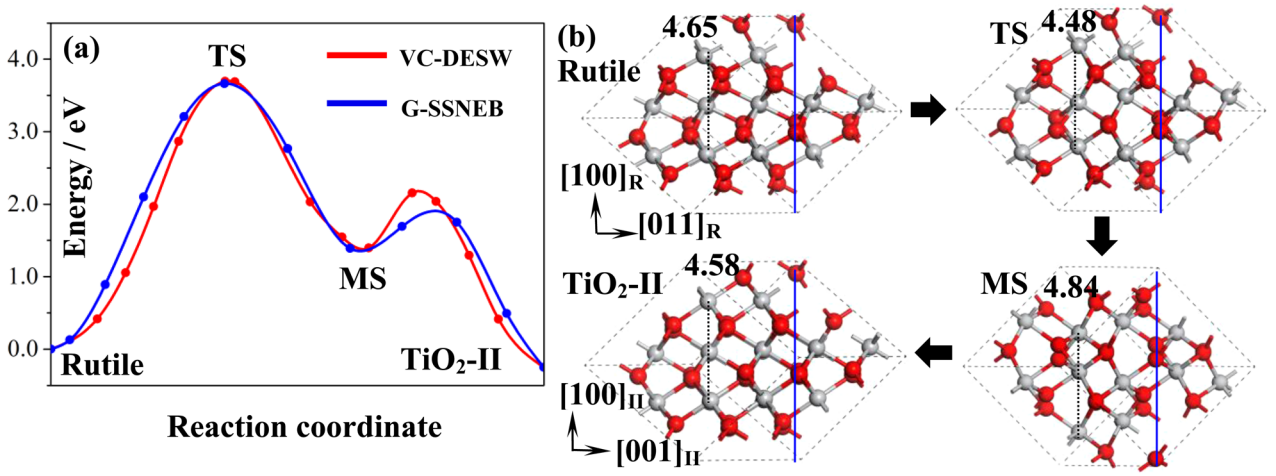

Figure 5. Reaction profile from VC-DESW (red line) and G-SSNEB (blue line) together with the key structures. The blue lines in the structures indicates the atomic habit plane edge, i.e., $(011)_R//(001)_{II}$. The labeled Ti−Ti distance is in Å. Ti atom, gray ball; O atom, red ball.

being only 0.1 eV larger than the exact barrier, which indicates that the pseudopathway of VC-DESW can provide a good estimation to the reaction barrier. The subsequent single-ended CBD method takes another 78 steps to finally converge to the true TS.

$$\mathbf{X} = \frac{\mathbf{Q}^{FS} - \mathbf{Q}^{IS}}{\|\mathbf{Q}^{FS} - \mathbf{Q}^{IS}\|} \tag{29}$$

$$\mathbf{Y} = \frac{\mathbf{Q}^{TS} - \mathbf{Q}^{IS} - [(\mathbf{Q}^{TS} - \mathbf{Q}^{IS})\cdot\mathbf{X}]\mathbf{X}}{\|\mathbf{Q}^{TS} - \mathbf{Q}^{IS} - [(\mathbf{Q}^{TS} - \mathbf{Q}^{IS})\cdot\mathbf{X}]\mathbf{X}\|} \tag{30}$$

$$z = \|(\mathbf{Q} - \mathbf{Q}^{IS}) - [(\mathbf{Q} - \mathbf{Q}^{IS})\cdot\mathbf{X}]\mathbf{X} - [(\mathbf{Q} - \mathbf{Q}^{IS})\cdot\mathbf{Y}]\mathbf{Y}\| \tag{31}$$

We would like to emphasize that VC-DESW aims for quick TS location and is not an ideal tool for finding the MEP, as also discussed previously.[3] The MEP can be retrieved rigorously, if interested, using the obtained TS with alternative techniques, such as intrinsic reaction pathway (IRC) using the Gonzalez−Schlegel method[45] and the Ishida−Morokuma−-Komornicki method.[46] This will, however, significantly increase the computational cost. In practice, one can use the steep-descendent and BFGS combined local optimization technique to extrapolate the pathway starting from TS and confirm the TS in between the IS and FS. Using this approach, we found that it requires additional 149 force/energy evaluations to build the whole pathway for TiO_2-B-to-anatase phase transition and thus the total force/energy evaluation step (343) is already similar to that of the G-SSNEB method to converge the pathway close to the MEP (N_{img} = 10, 380 steps, Table 1).

3.1.2. Rutile-to-TO_2-II Phase Transition. The reaction energy profile for the rutile-to-TO_2-II phase transition is shown in Figure 5a, and the key structures involved in the reaction are shown in Figure 5b. The phase transition obeys the crystallographic orientation relationship $(011)_R//(001)_{II}$; $[100]_R//[100]_{II}$.[25,35] There are appreciable movements on O atoms in the phase transition. Both VC-DESW and G-SSNEB identify an intermediate phase (Baddeleyite, $P21/c$, a = 4.87 Å, b = 4.91 Å, c = 5.09 Å, $\alpha = \gamma = 90°$, β = 100.4°, and Z = 4) and therefore the pathway involves two elementary steps. The rutile-to-Baddeleyite transition dictates the highest energy position in the pathway. As shown in Table 1, the VC-DESW takes 228 steps to locate the TS, whereas the G-SSNEB takes 300−680 steps in total (6 and 10 images) to find the TS.

By comparing the pathways from two methods (Figure 5a), we found that the pseudopathway from VC-DESW mimics closely the converged MEP from the G-SSNEB method. In particular, the estimated barrier from the highest energy point of the pseudopathway of VC-DESW is almost identical to the exact barrier (<0.01 eV). Consistently, the dominant cost for the TS location using the VC-DESW method is in pseudopathway building, 199 steps, and the CBD steps for TS location only needs 27 steps.

If one is interested in the whole pathway including the second TS along the pathway, the extrapolation from the TS to the IS/FS must be carried out, and the second TS needs to be searched similarly using VC-DESW. This will certainly require additional force/energy evaluation steps. For the Rutile-to-TO_2-II phase transition, it takes an additional 346 steps in total, including 221 steps for the extrapolation from two TSs and 125 steps for the location of the second TS using VC-DESW. In fact, for the pathway sampling shown below, where the detailed pathway information is not required in general, such computational efforts can be largely saved by using the VC-DESW method.

3.2. Phase Transition of SiO_2 from α-Quartz to the Quartz-II Phase. Because the VC-DESW method is particularly suitable for the fast assessment of the solid phase transition barrier, it allows for a large-scale screening of the solid phase transition pathways and the identification of the low energy pathway when combining with the SSW crystal pathway sampling method.[24] Here, we chose silica (SiO_2) as the model system to illustrate the unique functionality of the SSW/VC-DESW approach[26] for resolving the solid phase transition mechanism.

Silica is the abundant matter in the earth crust, and its phase transition under high pressure has been of great scientific interest.[10] While silica has many different phases, the phase transition from α-quartz to the quartz-II phase is one of the most studied in both experiments and theory.[47,48] It is known that the phase transition occurs at 22 GPa at 300 K.[48] Theoretically, although it has been studied using metadynamics and Parrinello−Rahman methods,[10,30−34,49] the detailed mechanism and the reaction energetics remain uncertain.

DOI: 10.1021/acs.jctc.5b00641
J. Chem. Theory Comput. 2015, 11, 4885−4894

Following previous theoretical work,[13,24,47] we use the Beest−Kramer−van Santen (BKS) potential[50] to describe the PES of silica, which has been shown to reproduce the structure of α-quartz ($P3_121$, $a = b = 4.75$ Å, $c = 5.39$ Å, $\alpha = \beta = 90°$, $\gamma = 120°$, and $Z = 3$) and the quartz-II phase (C2, $a = 8.68$ Å, $b = 3.41$ Å, $c = 5.51$ Å, $\alpha = \gamma = 90°$, $\beta = 112.4°$, and $Z = 6$) phase at ∼5 GPa by comparing with experimental and quantum mechanics calculations.[47] To demonstrate the ability of the SSW/VC-DESW method for resolving the high barrier solid phase transition reaction, we have performed the SSW reaction pathway sampling at relatively low pressure conditions, i.e., 5 GPa. The pressure dependence of the phase transition is then studied by changing the pressure of the lowest energy pathway.

In our simulation, we first utilize the SSW crystal pathway sampling method to collect the likely pathways from α-quartz to quartz-II at 5 GPa. The SSW crystal pathway sampling method[24] starts from the α-quartz phase and explores the likely product phases nearby. All of the product phases that are different from α-quartz will be recorded, which yields a database of IS/FS pairs (IS is the α-quartz phase, and the FS is the product phase). In this work, we collected 52 pathways that take 8612 force/energy evaluation steps, and 26 of them are related to the α-quartz to quartz-II transition. The SSW simulation parameters utilized are the same as those used in the previous work.[24] Next, we utilize the VC-DESW method to establish the pseudopathway for the 26 IS/FS pairs related to the α-quartz to quartz-II transition and finally locate the TS of these pathways.

All of the 26 pathways belong to the same lowest energy pathway (with identical TS), and the calculated reaction barrier is 0.65 eV per 36 atoms. Overall, it takes 20551 energy/force evaluation steps to locate the TSs of all 26 reaction pathways (on average, 790 steps for each TS with a stringent convergence criterion, 0.005 eV/Å and 0.005 GPa for the maximum force on atom and the stress, respectively; Table 2). In total, 29163 energy/force evaluation steps are required to resolve the lowest energy pathway. We note that a significant amount of computational time is spent on few high energy pathways that have a long distance between IS and FS, which can in fact be terminated early if extra screening conditions on the energy barrier are applied.

Table 2. Force Evaluation Steps (N_{force}) and the Number of Pathways (N_{path}) Identified for SiO_2 Homogeneous Phase Transition from α-Quartz to the Quartz-II Phase by the SSW/VC-DESW Pathway Sampling Method

	SSW	VC-DESW
N_{force}	8612	20551
N_{path}	52 (26)[a]	26[b]

[a]The total number of IS/FS pairs and those (in parentheses) related to the α-quartz to quartz-II transition. [b]All of the pathways identified from α-quartz to quartz-II belong to the same lowest energy pathway.

Using metadynamics, Martoňák et al. have identified a reaction pathway for the phase transition, which requires 88 metasteps (each consisting of a 5 ps MD run). It should be mentioned that due to the extra constraints applied on all six degrees of freedom of the lattice in metadynamics, the pathway observed from metadynamics is not exactly the same as our identified lowest energy pathway.

Here, we describe briefly the mechanism of the α-quartz to quartz-II transition based on the lowest energy pathway. The snapshots of the pathway are displayed in Figure 6. We note that the phase transition involves a large volume drop (28.6%, from 421.36 Å^3 to 301.30 Å^3) with a maximal principal compression along the [100] direction (a axis from 9.56 to6.81 Å). The lattice also experiences a large distortion with the α angle from 90° to 69°. This indicates that the α-quartz to quartz-II transition belongs to the reconstructive phase transition instead of the diffusionless Martensitic phase transition. In accordance with the large volume decrease, the coordination number of Si changes appreciably: two-thirds of Si atoms increases the coordination from 4-fold to 6-fold. As shown in Figure 6a where one layer polyhedrons are labeled as **1−6**, the **3−6** polyhedrons transform from 4-fold to 6-fold coordination with edge sharing. The remaining 4-fold Si also changes their coordination environment: the tetrahedron SiO_4 structure is distorted, and an O−Si−O angle reduces from 109.8° to 102.3°.

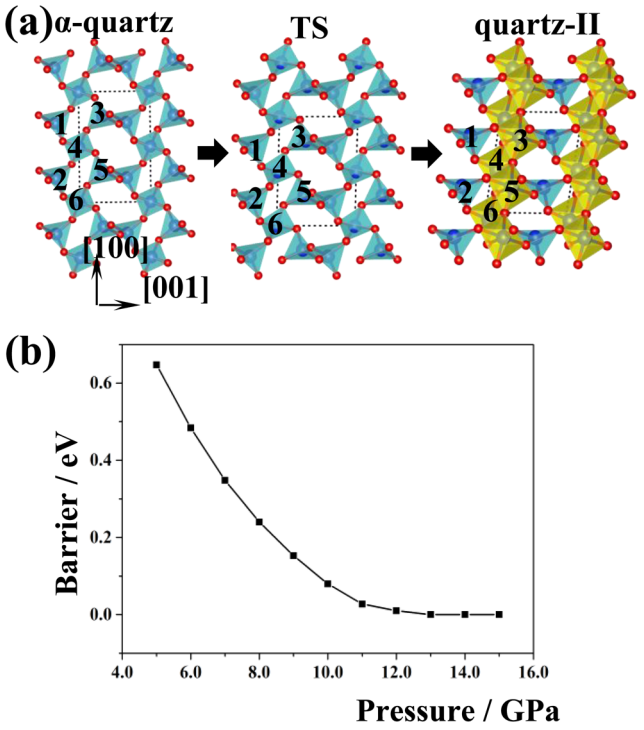

Figure 6. (a) Lowest energy phase transition pathways from α-quartz to quartz-II phase obtained using SSW/VC-DESW pathway sampling. Light blue polyhedrons, 4-fold coordination SiO_4; deep blue polyhedrons, 6-fold coordination SiO_6. (b) Reaction barriers for the α-quartz to quartz-II phase transition under different pressures.

Finally, we also investigated the pressure dependence of the phase transition. The phase transition occurs in experiments at ∼22 GPa, which is higher than the 5 GPa studied in this work. We compute the barrier of the lowest energy pathway using the VC-DESW method under different pressures, and the results are shown in Figure 6b. We found that the reaction barrier (per 36 atoms) decreases smoothly with the increase of the external pressure and that the phase transition becomes a barrierless process above 13.0 GPa. Obviously, this indicates that the empirical potential underestimates the barrier height systematically and that the predicted transition pressure is too low (∼10 GPa) compared to the experimental value. In our ongoing work, the DFT-based pathway sampling and TS

DOI: 10.1021/acs.jctc.5b00641
J. Chem. Theory Comput. 2015, 11, 4885−4894

location are utilized to further verify the mechanism of SiO_2 phase transition.

4. CONCLUSIONS

This work develops a variable-cell version of the double-ended surface walking method for locating TS in solid phase transition. We describe the detailed algorithm of the new method and focus particularly on the generalized coordinate that includes both the lattice and atom degrees of freedom. This generalized coordinate system with a scaled fractional coordinate on the atom is lattice rotation invariant and can efficiently couple the lattice and atom displacement to yield soft eigenstates of Hessian. We demonstrate this new method in two complex phase transition systems and show that the method is highly efficient for TS location. We also combine the method with the SSW crystal pathway sampling to reveal the phase transition pathway of SiO_2 under high pressure. Our work shows that automated pathway sampling together with the quick TS location can greatly facilitate the understanding of solid state phase transition and the prediction of the stability of crystals. We expect that this combination approach would be applicable for the rational design of new material via large-scale computational simulation.

■ ASSOCIATED CONTENT

Supporting Information

The Supporting Information is available free of charge on the ACS Publications website at DOI: 10.1021/acs.jctc.5b00641.

Performance of VC-DESW in different supercells in TiO_2-B-to-anatase transition; phonon spectrum and 3N +3 eigenvalues for the TS in TiO_2-B-to-anatase transition; and XYZ coordinates for all of the pathways reported in this work (PDF)

■ AUTHOR INFORMATION

Corresponding Author

*E-mail: zpliu@fudan.edu.cn.

Funding

This work was supported by National Science Foundation of China (21173051, 21361130019, and 21533001), 973 program (2011CB808500 and 2013CB834603), Science and Technology Commission of Shanghai Municipality (08DZ2270500), and Program for Professor of Special Appointment (Eastern Scholar) at Shanghai Institute of Higher Learning.

Notes

The authors declare no competing financial interest.

■ REFERENCES

(1) Schlegel, H. B. *WIREs Comput. Mol. Sci.* **2011**, *1*, 790−809.
(2) Chill, S. T.; Stevenson, J.; Ruehle, V.; Shang, C.; Xiao, P.; Farrell, J. D.; Wales, D. J.; Henkelman, G. *J. Chem. Theory Comput.* **2014**, *10*, 5476−5482.
(3) Zhang, X.-J.; Shang, C.; Liu, Z.-P. *J. Chem. Theory Comput.* **2013**, *9*, 5745−5753.
(4) Smirnov, M.; Mirgorodsky, A.; Guinebretière, R. *Phys. Rev. B: Condens. Matter Mater. Phys.* **2003**, *68*, 104106.
(5) Parrinello, M.; Rahman, A. *Phys. Rev. Lett.* **1980**, *45*, 1196−1199.
(6) Parrinello, M.; Rahman, A. *J. Appl. Phys.* **1981**, *52*, 7182−7190.
(7) Parrinello, M.; Rahman, A.; Vashishta, P. *Phys. Rev. Lett.* **1983**, *50*, 1073−1076.
(8) Focher, P.; Chiarotti, G. L.; Bernasconi, M.; Tosatti, E.; Parrinello, M. *Europhy. Lett.* **1994**, *26*, 345.
(9) Dellago, C.; Bolhuis, P. G.; Csajka, F. S.; Chandler, D. *J. Chem. Phys.* **1998**, *108*, 1964−1977.
(10) Zahn, D.; Hochrein, O.; Leoni, S. *Phys. Rev. B: Condens. Matter Mater. Phys.* **2005**, *72*, 094106.
(11) Dellago, C.; Bolhuis, P. Transition Path Sampling and Other Advanced Simulation Techniques for Rare Events. In *Advanced Computer Simulation Approaches for Soft Matter Sciences III*; Holm, C., Kremer, K., Eds. Springer: Berlin, Germany, 2009; Vol. *221*, pp 167−233.
(12) Martoňák, R.; Laio, A.; Parrinello, M. *Phys. Rev. Lett.* **2003**, *90*, 075503.
(13) Martonak, R.; Donadio, D.; Oganov, A. R.; Parrinello, M. *Nat. Mater.* **2006**, *5*, 623−626.
(14) Zhu, Q.; Oganov, A. R.; Lyakhov, A. O. *CrystEngComm* **2012**, *14*, 3596−3601.
(15) Oganov, A. R.; Martonak, R.; Laio, A.; Raiteri, P.; Parrinello, M. *Nature* **2005**, *438*, 1142−1144.
(16) Sun, J.; Klug, D. D.; Martoňák, R.; Montoya, J. A.; Lee, M.-S.; Scandolo, S.; Tosatti, E. *Proc. Natl. Acad. Sci. U. S. A.* **2009**, *106*, 6077−6081.
(17) Wang, H.-F.; Liu, Z.-P. *J. Am. Chem. Soc.* **2008**, *130*, 10996−11004.
(18) Shang, C.; Liu, Z.-P. *J. Am. Chem. Soc.* **2011**, *133*, 9938−9947.
(19) Trinkle, D. R.; Hennig, R. G.; Srinivasan, S. G.; Hatch, D. M.; Jones, M. D.; Stokes, H. T.; Albers, R. C.; Wilkins, J. W. *Phys. Rev. Lett.* **2003**, *91*, 025701.
(20) Hennig, R. G.; Trinkle, D. R.; Bouchet, J.; Srinivasan, S. G.; Albers, R. C.; Wilkins, J. W. *Nat. Mater.* **2005**, *4*, 129−133.
(21) Caspersen, K. J.; Carter, E. A. *Proc. Natl. Acad. Sci. U. S. A.* **2005**, *102*, 6738−6743.
(22) Sheppard, D.; Xiao, P.; Chemelewski, W.; Johnson, D. D.; Henkelman, G. *J. Chem. Phys.* **2012**, *136*, 074103.
(23) Shang, C.; Liu, Z.-P. *J. Chem. Theory Comput.* **2013**, *9*, 1838−1845.
(24) Shang, C.; Zhang, X.-J.; Liu, Z.-P. *Phys. Chem. Chem. Phys.* **2014**, *16*, 17845−17856.
(25) Zhu, S.-C.; Xie, S.-H.; Liu, Z.-P. *J. Phys. Chem. Lett.* **2014**, *5*, 3162−3168.
(26) Guan, S.-H.; Zhang, X.-J.; Liu, Z.-P. *J. Am. Chem. Soc.* **2015**, *137*, 8010−8013.
(27) Shang, C.; Liu, Z.-P. *J. Chem. Theory Comput.* **2012**, *8*, 2215−2222.
(28) Shang, C.; Liu, Z.-P. *J. Chem. Theory Comput.* **2010**, *6*, 1136−1144.
(29) Henkelman, G.; Jonsson, H. *J. Chem. Phys.* **1999**, *111*, 7010−7022.
(30) Munro, L. J.; Wales, D. J. *Phys. Rev. B: Condens. Matter Mater. Phys.* **1999**, *59*, 3969−3980.
(31) Matsui, M.; Akaogi, M. *Mol. Simul.* **1991**, *6*, 239−244.
(32) Souza, I.; Martins, J. *Phys. Rev. B: Condens. Matter Mater. Phys.* **1997**, *55*, 8733−8742.
(33) Zhu, S.-C.; Guan, S.-H.; Zhao, W.-N.; Liu, Z.-P. *Top. Catal.* **2015**, *58*, 644.
(34) Zhao, W.-N.; Zhu, S.-C.; Li, Y.-F.; Liu, Z.-P. *Chem. Sci.* **2015**, *6*, 3483−3494.
(35) Shang, C.; Zhao, W.-N.; Liu, Z.-P. *J. Phys.: Condens. Matter* **2015**, *27*, 134203.
(36) Zhou, W.; Gai, L.; Hu, P.; Cui, J.; Liu, X.; Wang, D.; Li, G.; Jiang, H.; Liu, D.; Liu, H.; Wang, J. *CrystEngComm* **2011**, *13*, 6643−6649.
(37) Yang, D.; Liu, H.; Zheng, Z.; Yuan, Y.; Zhao, J.-c.; Waclawik, E. R.; Ke, X.; Zhu, H. *J. Am. Chem. Soc.* **2009**, *131*, 17885−17893.
(38) Sheppard, D.; Xiao, P.; Chemelewski, W.; Johnson, D. D.; Henkelman, G. Transition State Tools for VASP. http://theory.cm.utexas.edu/vtsttools/ (accessed May 10, 2015).
(39) Kresse, G.; Hafner, J. *Phys. Rev. B: Condens. Matter Mater. Phys.* **1993**, *47*, 558−561.
(40) Kresse, G.; Furthmüller, J. *Comput. Mater. Sci.* **1996**, *6*, 15−50.

DOI: 10.1021/acs.jctc.5b00641
J. Chem. Theory Comput. 2015, 11, 4885−4894

(41) Kresse, G.; Joubert, D. *Phys. Rev. B: Condens. Matter Mater. Phys.* **1999**, *59*, 1758−1775.
(42) Perdew, J. P.; Burke, K.; Ernzerhof, M. *Phys. Rev. Lett.* **1996**, *77*, 3865−3868.
(43) Monkhorst, H. J.; Pack, J. D. *Phys. Rev. B: Condens. Matter Mater. Phys.* **1976**, *13*, 5188−5192.
(44) Bitzek, E.; Koskinen, P.; Gähler, F.; Moseler, M.; Gumbsch, P. *Phys. Rev. Lett.* **2006**, *97*, 170201.
(45) Gonzalez, C.; Schlegel, H. B. *J. Phys. Chem.* **1990**, *94*, 5523−5527.
(46) Ishida, K.; Morokuma, K.; Komornicki, A. *J. Chem. Phys.* **1977**, *66*, 2153−2156.
(47) Campañá, C.; Müser, M. H.; Tse, J. S.; Herzbach, D.; Schöffel, P. *Phys. Rev. B: Condens. Matter Mater. Phys.* **2004**, *70*, 224101.
(48) Kingma, K. J.; Hemley, R. J.; Mao, H.-k.; Veblen, D. R. *Phys. Rev. Lett.* **1993**, *70*, 3927−3930.
(49) Huang, L.; Durandurdu, M.; Kieffer, J. *Nat. Mater.* **2006**, *5*, 977−981.
(50) van Beest, B. W. H.; Kramer, G. J.; van Santen, R. A. *Phys. Rev. Lett.* **1990**, *64*, 1955−1958.

DOI: 10.1021/acs.jctc.5b00641
J. Chem. Theory Comput. 2015, 11, 4885−4894